# Transient Wavelet Energy Based Protection Scheme for Inverter-Dominated Microgrid

Di Liu, Adam Dyśko, *Member, IEEE,* Qiteng Hong, *Senior Member, IEEE,* Dimitrios Tzelepis, *Member, IEEE,* and Campbell Booth

***Abstract*—When faults occur in the microgrids, high frequency transients will be superimposed on the system currents and voltages. The magnitude of those transients will attenuate as it encounters the discontinuity points in the network such as busbars, or any other impedance discontinuity points. This phenomenon can also be quantified by wavelet energy, which provides a useful tool to detect faults and locate the faulted feeder in the microgrid. In this paper, a novel protection scheme based on the transient wavelet energy of the superimposed current extracted by the Maximal Overlap Discrete Wavelet Transform (MODWT) algorithm is developed to detect faults and locate the faulted feeder in microgrids. Compared with existing protection schemes, the proposed protection scheme has the advantage of being largely immune to the changes in system fault level, fault types and positions, microgrid operating status and the control strategies deployed on the inverters, while presenting much lower requirement on the sampling frequency (10 kHz) compared with travelling wave-based methods. Unlike the conventional differential protection, the proposed scheme does not require synchronized measurement or high bandwidth communication channels, and thus, it can be considered as an economical and promising solution for microgrids.**

***Index Terms*—Inverter dominated microgrid, microgrid protection, transient based protection, wavelet energy.**

NOMENCLATURE

| | |
|---|---|
| $E_j$ | $j^{th}$ individual wavelet energy |
| $E^p_{j,CT_n}$ | $j^{th}$ three-phase individual wavelet energies of $CT_n$ |
| $\Delta I^p_{CT_n}$ | three-phase superimposed currents of $CT_n$ |
| $TWE_j$ | $j^{th}$ transient wavelet energy |
| $TWE^p_{j,CT_n}$ | $j^{th}$ three-phase transient wavelet energies of $CT_n$ |
| $TWE^{p_{max}}_{j,CT_n}$ | $j^{th}$ maximum-phase transient wavelet energy of $CT_n$ |
| $TWE^{max}_j$ | $j^{th}$ maximum transient wavelet energy among all CTs at the certain busbar |
| $W_j$ | $j^{th}$ wavelet coefficient |
| $W^p_{j,CT_n}$ | $j^{th}$ three-phase wavelet coefficients of $CT_n$ |

## I. Introduction

MOTIVATED by the progress of the converter technology and the concern for the environment, the renewable energy based distributed generation (DG) has gained a significant increase in recent decades [1]. However, the large amounts of the interconnected DGs rise many issues related to the control and management of existing distribution networks. In this context, the concept of microgrid was proposed in [2] to integrate the DGs effectively through treating the DGs and loads together as a subsystem. Microgrid is a compact network comprising generators, loads and storage assets [3], which is commonly implemented at the consumers' end. In normal situation, a microgrid is typically connected to the main grid, but when severe disturbances occur, e.g. loss of major generation and faults, it can be safely disconnected from the main grid at the point of common coupling (PCC) and can run as an independent islanded system. This dual-mode capability of the microgrid strengthens the grid resilience and mitigates the risk of the power interruption [4]. However, it also poses significant challenges on the protection systems. As demonstrated in [5], the fault level of a microgrid can change dynamically in different operating modes. In the grid-connected mode, the fault level of the microgrid is typically high, owing to the infeed from the main grid. However, in the islanded mode, the fault level can reduce massively since the fault infeed is only contributed by the local DGs with relatively small capacity. The reduction and variation of the fault level will be particularly significant if the microgrid is dominated by the inverter-interfaced distributed generators (IIDGs). For this reason, faults in the microgrid are challenging to detect with high level of discrimination using the traditional current based protection which depends on large fault current magnitudes [6]. Furthermore, unlike the conventional synchronous generation, the fault behaviour of the IIDG is mainly governed by the embedded controller, which may have different fault responses, depending on the grid code of the specific country, adopted reference frame, and current limitation strategies [7]. These issues all contribute to the challenges in effective protection of a microgrid dominated by IIDGs.

Several protection schemes designed for microgrids have been proposed in the literature. One commonly found solution uses the concept of adaptive protection to deal with the varying fault levels [8] [9]. In such schemes, the protection relay setting is adjusted automatically based on the prevailing system conditions, and in this way, it is possible to cope with the fault level variation between different operating modes. However, advanced communication and monitoring systems are typically required in adaptive based schemes, which could present significant overall cost of the protection system. Additionally, the adaptive approach requires a good understanding of the real time condition of the studied network, and the relay setting process and validation can be very complicated. Another commonly suggested solution is to implement a differential scheme in the microgrid since it is less sensitive to the fault level variation [10]. However, such a scheme typically requires the synchronized measurement of currents at different

locations and relies on the high-bandwidth communications to transmit the three-phase current between the two ends of the feeder. The protection schemes based on the advanced signal processing tools and the artificial intelligence (AI) are proposed in [11] [12]. In these schemes, useful features of the fault signatures are extracted by the wavelet transform and then are used to train the AI-based scheme to distinguish and identify the fault. However, these techniques typically require large amounts of realistic training data, which are often not available. Another group of microgrid protection schemes is the active protection approach, where the protection algorithm is assisted by the active control of IIDGs during the faults. For example, in [13] [14], the pre-defined harmonic currents are injected by the IIDGs into the microgrid during the fault period to select the faulted feeder. One advantage of the active approach is that it is based on the designed fault features created intentionally by the generator rather than the current or voltage at the fundamental frequency, and therefore, it can potentially be independent of the fault level changes. However, this approach requires the modification of the IIDGs controllers and the control algorithm must be carefully designed to match the protection requirements, which can be difficult to realise in the inverters from the different vendors. To minimize the negative impacts caused by the reduced fault level and nonuniform control strategies of inverters, the method proposed in [15] uses a travelling wave-based approach to protect a 20 kV microgrid. However, the method needs a relatively high sampling frequency (at least 256 kHz). Additionally, the sampling frequency will increase further with the decrease of the feeder's length.

As the microgrid is typically implemented in the distribution system, where the feeder length is very short (typically hundreds of meters in a 400 V network), this makes the implementation of traditional travelling-wave methods extremely challenging owing to the high requirements on the sampling frequency. Additionally, due to the short distance, the travelling wave methods will typically experience issues on distinguishing the initial and reflected waves clearly because of the frequent waves reflections between the fault point and neighbouring terminals [16].

To address the aforementioned challenges of applying conventional current-based protection due to fault level changes, adaptive protection due to the high requirement on advanced communication and monitoring infrastructure, AI-based protection due to the need for realistic training data, and travelling wave-based methods due to the need for high sampling frequency, this paper presents a novel protection algorithm based on the transient wavelet energy of superimposed current, which is capable of effectively detecting faults and locating the faulted feeder in microgrids. It has been found that, when faults occur in the microgrids, for the current transformers (CTs) connected to the same bus, the wavelet energy of the CT closest to the fault has the highest magnitude, and the magnitude will attenuate as it encounters the discontinuity points in the network such as busbars, or any other impedance discontinuity points. This phenomenon can be quantified by wavelet energy, which provides a useful tool to detect faults and locate the faulted feeder in the microgrid. Additionally, as the transient based protection uses the high frequency transients caused by faults rather than the fundamental frequency components created by the generators, therefore, it can be largely unaffected by the fault level changes and different control algorithms implemented by IIDGs. The Maximal Overlap Discrete Wavelet Transform (MODWT) [17] is employed in the paper to extract the wavelet coefficients owing to its high performance in transient analysis. It should be noted that for microgrid protection, the main objective is identifying the faulted feeder rather than estimating the fault position within a feeder accurately as in the case of long transmission lines. For these reasons, the wavelet energy based protection scheme relying on the energy of the fault induced current rather than the wavefront of travelling wave, is developed in this paper, which significantly reduces the sampling frequency requirement of the relay. Furthermore, considering the large amounts of the single-phase loads in the microgrid and the future requirement for single-phase tripping capability [18], a fault classification strategy for selecting the faulted phase in the case of a single phase-to-ground fault, is also introduced.

The key advantages of the proposed protection method can be summarized as follows:

1) The proposed method is capable of protecting microgrids under both grid connected and islanded modes without the need for changing the settings and is not impacted by the control methods of the IIDGs.
2) The required sampling frequency of this scheme is around 10 kHz, which is significantly lower than conventional travelling wave-based methods (e.g. over 200 kHz in [15]).
3) The proposed scheme does not need the high-bandwidth communications as traditional differential protection.
4) The protection scheme supports the single-phase tripping capability and it can protect the branch feeders with single-ended measuring devices.

The rest of this paper is organized as follows: Section II reviews the fundamentals of the fault-induced high-frequency transients, the definition of the transient wavelet energy (TWE) and explains the energy relationship of the CTs connected to the same busbar. Section III presents the design of the proposed transient wavelet energy based protection scheme. Section IV presents the case studies that evaluate the performance of the proposed scheme using a CIGRE benchmark microgrid. Conclusions of the work are provided in Section V.

## II. FAULT-INDUCED TRANSIENTS AND TRANSIENT WAVELET ENERGY

### A. Fundamentals of Fault-Induced High-Frequency Transients

According to the Thevenin's and superposition theorem, the faulted network can be represented as the sum of the pre-fault network and the superimposed network [19] as shown in Fig. 1, where the $E_1$ and $E_2$ stand for the pre-fault voltage sources in the network; $V_{pre}$ is the pre-fault voltage at at the fault point; $Z_{S1}$ and $Z_{S2}$ are the internal impedances of the voltage sources $E_1$ and $E_2$; $Z_L$ is the line impedance; $R_F$ is the fault resistance; $\Delta V$ is the superimposed voltage at the fault point, and $\Delta I$ is the

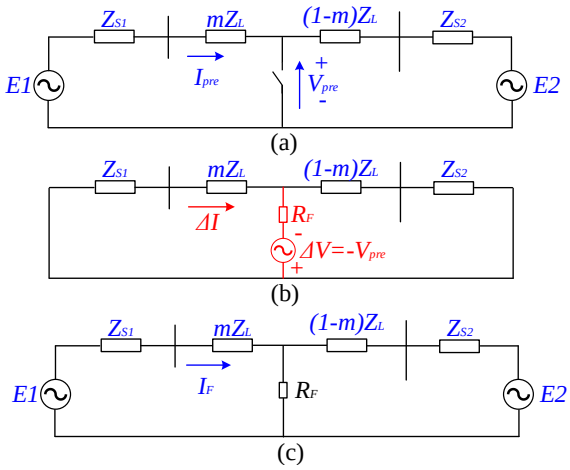


Fig. 1. Diagram used to display, (a) pre-fault network, (b) superimposed network, (c) faulted network.

current flowing in the superimposed network. The magnitude of $\Delta V$ equals to the magnitude of pre-fault voltage at the fault position, while the voltage polarity of $\Delta V$ is opposite to the pre-fault voltage [20]. Additionally, as presented in Fig. 1 (b), the superimposed currents flowing in the network are driven by the superimposed voltage source, $\Delta V$, at the fault position, which is the only active source in the superimposed network [20].

As reported in [21], the term 'superimposed current' is relatively broad and can be further categorised into different types based on the filtering or processing applied in the protection system to obtain specific features. In this paper, the fault-induced high-frequency transients of superimposed currents are extracted by the high-pass filters in the MODWT algorithm, whose magnitude is mainly dependent on the system topology and the fault parameters such as fault inception angle and fault resistance [22].

One thing needs to be further clarified is that the observed transients are not travelling waves, which result from the reflections of current and voltage wavefronts travelling along the lines [22]. As explained in [23], at the initial stage of fault, the network behaves as a distributed parameter system, where the travelling waves propagate and reflect in the network. After multiple reflections, the travelling waves recombine into a stationary signal, and the network evolves into a transient-state lumped parameter network, where the analysed high-frequency transients appear. In travelling wave based methods, the exact arrival time of the wavefront is typically required to localise the fault. Given the fast propagation of travelling waves (close to the speed of light), a very high sampling frequency is necessary to capture the accurate time information of the arriving wavefronts [24] (i.e. in MHz range). However, in the protection scheme presented in this paper, only the energy information is required and the employed high-frequency transients are available within a few milliseconds after the fault inception [21].

The typical waveform of fault current and its frequency spectrum are presented in Fig. 2. The fundamental frequency of the FFT analysis is set as 1 kHz and given the fast attenuation of high-frequency transients, the signal of 1 ms

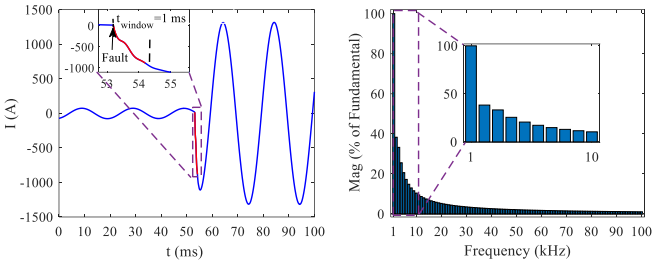


Fig. 2. Fault current waveform and frequency spectrum of fault-induced high-frequency transients.

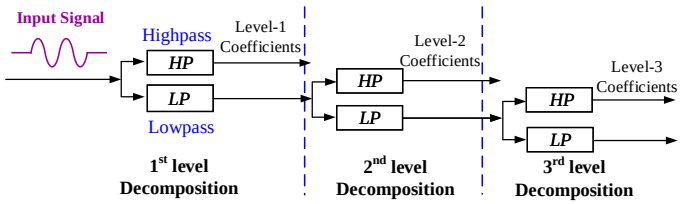


Fig. 3. 3-level MODWT decomposation diagram.

duration following the fault inception is analysed. In Fig. 2, the magnitude spectrum is shown as a percentage of the magnitude of the fundamental frequency, i.e., 1 kHz in this case. Based on the FFT results in Fig. 2, the frequency spectrum of fault-induced high-frequency content ranges widely. It is evident that the frequencies below 10 kHz contain sufficient fault signature information. Therefore, sampling at 10 kHz is considered sufficient to analyse the fault-induced transients used in the paper and such sampling frequency is feasible to be implemented on a conventional numerical relay [25].

### *B. Definition of the Transient Wavelet Energy*

Wavelet Transform (WT) is a powerful processing tool particularly suitable for the analysis of non-stationary signals [26]. MODWT is a variant of Discrete Wavelet Transform (DWT) without the down-sampling procedure (a 3-level decomposition algorithm is illustrated in Fig. 3 as an example), and it can be used to realize a faster fault detection than the DWT based methods [27]. In this paper, the db4 mother wavelet is implemented to design the high-pass and low-pass filters in the MODWT algorithm due to its satisfactory performance in the analysis of the short and fast transient disturbances [28]. The level-1 wavelet coefficients from the high-pass filter are employed to decrease the computation and memory burden in the numerical relays. The sampling frequency of the developed protection system is 10 kHz, which is considered to be sufficient for extracting the high frequency components of interest and feasible to implement for the advanced numerical relays. Based on [29], the energy of the individual wavelet coefficient is calculated by (1).

$$E_j = W_j^2 \tag{1}$$

where the wavelet coefficients at the first decomposition level are used in the proposed scheme; the index $j$ is used to denote the $j^{th}$ wavelet coefficient at level 1, which is the

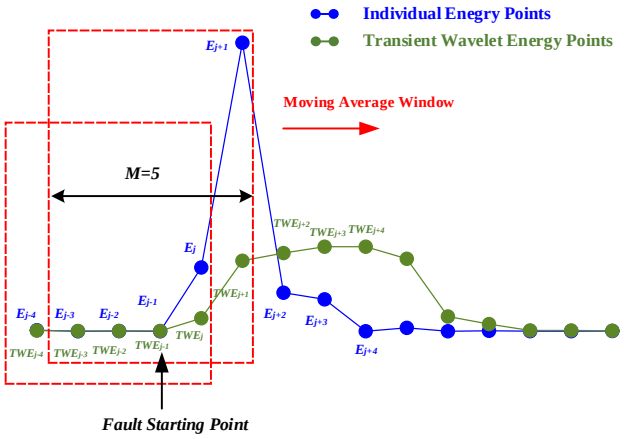


Fig. 4. Moving average window of the energy of individual wavelet coefficient.

most recent coefficient. The energy of an individual wavelet coefficient as represented in (1) can be sensitive to the system noise. To mitigate potential protection instability issue, a moving-average window is applied to smooth the short-time fluctuations of the energy. Therefore, the transient wavelet energy, $TWE_j$, after applying a moving average window, is defined as (2). This process is illustrated by Fig. 4.

$$TWE_j = \frac{E_j + E_{j-1} + \cdots + E_{j-M+1}}{M} = \frac{1}{M}\sum_{i=j-M+1}^{j} E_i \quad (2)$$

where $M$ is the length of the moving-average window. For a shorter window length, a higher protection sensitivity can be achieved, but it can also increase the risk of maloperation caused by noise. Based on the simulation, it was found that the main energy of transients is concentrated in the initial five samples after the fault inception, i.e., the $E_j$ to $E_{j+4}$ in Fig. 4. For this reason, the moving-average window with the length of $M = 5$ was implemented. It provides good trade-off between noise smoothing performance and speed of operation.

### C. Relationship of the Transient Wavelet Energy

The superimposed circuit of a typical busbar in a microgrid is shown in Fig. 5, where $L_1$ to $L_N$ stand for the feeders connected at the busbar, $Z_1$ to $Z_N$ are equivalent impedance of the feeders and $CT_1$ to $CT_N$ are the CTs installed at the terminals. In the case of the fault at $L_1$, the superimposed voltage source, $\Delta V$, which has the same magnitude but opposite polarity to the pre-fault voltage at that point, is applied at the fault position and the superimposed currents, $\Delta I_{CT_1}$ to $\Delta I_{CT_N}$, are introduced into the feeders. The assumed convention here is that the superimposed currents flowing away from the busbar have a positive value. It should be noted that the following derivation applies to the superimposed network only, and the conclusion is not necessary true for the pre-fault or faulted network.

Based on the research in [30], the polarity of superimposed current on the faulted feeder is opposite to the currents on the healthy feeder connected at the same busbar. According to the Kirchhoff's Current Law (KCL), the relationship of the superimposed currents in Fig. 5 can be described by (3), where

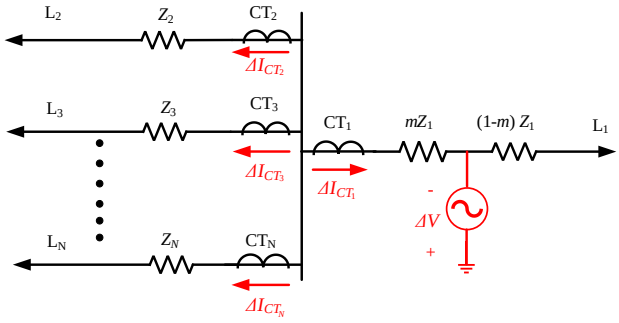


Fig. 5. Superimposed circuit for the fault at a feeder connected to a busbar.

'$p$' refers to the phase A, B and C and $k$ is the index of CTs connected to the same busbar.

$$\Delta I^p_{CT_1}(t) = -\sum_{k=2}^{N} \Delta I^p_{CT_k}(t) \quad (3)$$

In this study, the MODWT algorithm is implemented by the Discrete Finite Impulse Response (FIR) Filter [31], where the wavelet coefficients are extracted by convolving the sampled phase current with the coefficients of the designed high-pass filter [32]. As the filters used in that scheme have fixed coefficients, after applying the same FIR filter to both sides of the equation (3), the relationship of the input currents can also be expressed by the decomposed wavelet coefficients as indicated by (4).

$$W^p_{j,CT_1} = -\sum_{k=2}^{N} W^p_{j,CT_k} \quad (4)$$

From (4), the coefficient magnitude of the CT closest to the fault equals the sum of the CTs on the other branches, therefore, the energy of the CT on the fault side should be larger than the energy of any of the other CTs at the same busbar, which is depicted as (5). After applying moving average operation to (5), the inequality (6) can be derived.

$$E^p_{j,CT_1} > E^p_{j,CT_k}, k = 2, \cdots, N \quad (5)$$

$$TWE^p_{j,CT_1} > TWE^p_{j,CT_k}, k = 2, \cdots, N \quad (6)$$

To simplify the design and implementation of the protection algorithm, the maximum phase TWE is selected in this protection scheme. After simplification, the energy of the CTs at the same busbar is described as (7), where the $TWE^{p_{max}}_{j,CT_1}$ and $TWE^{p_{max}}_{j,CT_k}$ are the maximum-phase TWE of $CT_1$ and $CT_k$ respectively. For example, in the event of phase-A-to-ground fault, the energy of phase A will be largest, therefore, the $p_{max}$ in (7) refer to the energy of phase A.

$$TWE^{p_{max}}_{j,CT_1} > TWE^{p_{max}}_{j,CT_k}, k = 2, \cdots, N \quad (7)$$

According to (7), for the CTs connected at the same busbar, the CT closest to the fault has the largest TWE, which provides a useful indicator for locating the faulted feeder in the microgrid. The relation (7) can also be explained from energy conservation perspective. As shown in Fig.1 (b), the

only source of energy in the superimposed network is the fault-induced voltage source at the fault position. The energy generated by this source will be dissipated to all other passive components in the network. Therefore, no individual passive component or circuit can ever absorb more energy than the one created at the point of fault. Consequently, the energy flowing from the direction of the fault is always the highest.

## III. DESIGN OF THE PROPOSED PROTECTION SCHEME

### *A. Selection and Isolation of the Faulted Feeder*

Two assumptions are made for the design of the protection algorithm. Firstly, for every busbar in the microgrid, one digital relay is installed to collect and analyse the three phase currents from all CTs of the feeders connected at that busbar. Secondly, the communication channels are available between the relays on the opposite ends of all protected lines. It should be stressed that although communication is needed for the developed protection system, unlike differential protection, which requires the communication of sampled current values, the proposed scheme only requires low-cost communication with small bandwidth since the transmitted information only has binary values, i.e. '1' or '0', which is feasible and economic to implement in microgrids based on [33].

The designed protection scheme has two stages. To facilitate the understanding of the proposed protection scheme, a simple but representative three-bus microgrid in Fig. 6 is used in the discussion. The flowchart of the main fault detection algorithm (Stage I) is presented in Fig. 7. In the following description, "main feeder" refers to a feeder connected between two busbars (with relays at both ends) as $L_1$ and $L_2$ in Fig. 6; A "branch feeder" refers to the feeder connected to a load or a generator only (with no relay on the opposite end) as $L_3$ to $L_5$ in Fig. 6. Firstly, the relay installed at the busbar will collect the three-phase currents from the CTs on all feeders connected at that busbar. Based on these input currents, the wavelet coefficients of the phase currents are calculated by the MODWT algorithm. Three-phase TWEs of different CTs, $TWE^{p}_{j,CT_n}$, could be calculated by (1) and (2). As discussed in the previous section, the maximum phase energies, $TWE^{p_{max}}_{j,CT_n}$, of all CTs in the network are selected to simplify the design of the real-time implementation of the protection algorithm. In the next step, the CTs in the network will be further grouped based on the connected busbar and the maximum energy of the CTs at the same busbar, $TWE^{max}_{j}$, is identified, which is then compared against a fixed minimum energy threshold, $TWE_{thr}$, introduced to prevent unwanted operation during normal operating state with likely presence of signal noise.

Additionally, considering the potential impact of the non-fault disturbances, e.g. load switching, or power variation of the generators, the second threshold, $I_{thr\_pe}$, is applied for the CTs located at the "branch feeders". In effect, for all "main feeders", the relay will output binary value of '1' to the CT's side with maximum energy, $TWE^{max}_{j}$, as long as the energy value is above the threshold $TWE_{thr}$, but when maximum energy feeder corresponds to a "branch feeder", both energy and current conditions need to be met as displayed in Fig. 7, where $I_{ins}$ is the instantaneous current measured by the CT

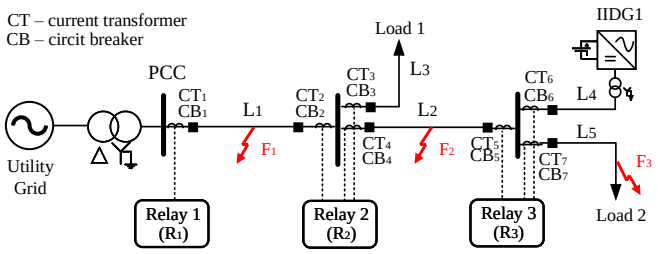


Fig. 6. Example of the three-bus simplified microgrid diagram used to illustrate the coordination principle.

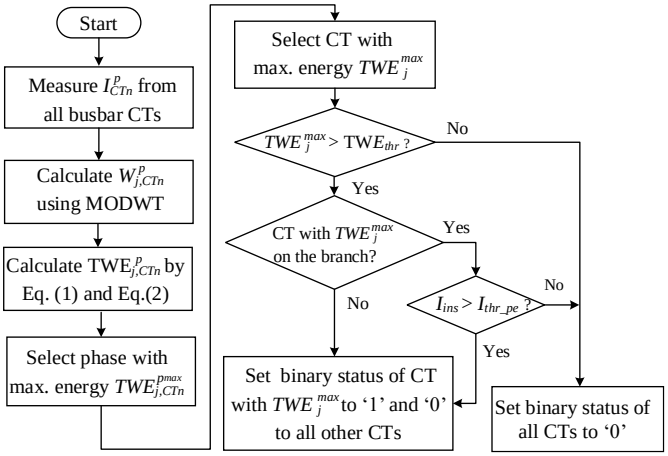


Fig. 7. Flowchart of the relay fault detection algorithm (Stage I).

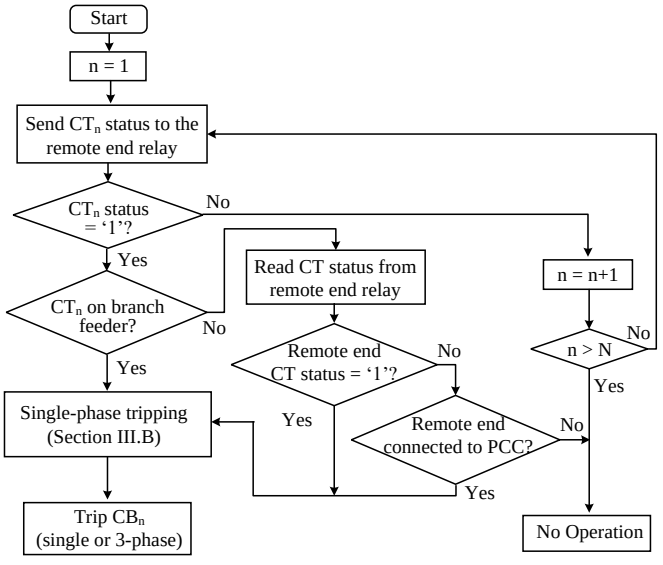


Fig. 8. Flowchart of the relay coordination algorithm (Stage II).

with $TWE^{max}_{j}$. This process is carried out by all relays in the microgrid.

The scheme tripping logic (Stage II) is shown in Fig. 8, where the variable '$n$' stands for the index of the CTs in the microgrid and $N$ is the total number of CTs. In that figure, the relays are coordinated based on the fault position in the microgrid and the CTs on the both terminals of the main feeder have the neighbouring index number. Three faults named $F_1$, $F_2$ and $F_3$ are applied to the microgrid in Fig. 6 to represent

the three fault scenarios, which are listed as follows.

1) $F_1$: Fault on a main feeder connected to PCC.
2) $F_2$: Fault on a main feeder not connected to PCC.
3) $F_3$: Fault on branch feeder.

According to the description in Section III.A, the status of CT with the maximum energy will be marked as '1' by local relay. For the faults $F_1$, $F_2$ and $F_3$ in Fig. 6, the binary outputs from the relays $R_1$, $R_2$ and $R_3$ are displayed in Table I.

From Table I, for the fault $F_1$ at the feeder connected with PCC, the binary value of $CT_2$ is always '1' in both grid-connected and islanded modes, while the binary value of $CT_1$ is '0' in islanded microgrid because the breaker at PCC is open. Based on the coordination strategy in Fig. 8, for the fault at main feeder connected to PCC, the relays, $R_1$ and $R_2$, will send tripping signal to $CB_1$ and $CB_2$ as long as the binary value of $CT_2$ is '1', therefore, the fault $F_1$ can be isolated in both-mode microgrids. Additionally, although the binary status of $CT_5$ are '1', while as the $CT_4$ sides are always '0' in both modes, the relays, $R_2$ and $R_3$, will not trip the $CB_4$ and $CB_5$ in the case of fault $F_1$. The other CBs, including $CB_3$, $CB_6$ and $CB_7$, at the branch feeders will also remain stable since the status values of $CT_3$, $CT_6$ and $CT_7$ sides are always '0' in the grid-connected and islanded microgrids. One point needs to be clarified is that for the coordination strategy in Fig. 8, no additional branch feeder is connected to the busbar at PCC, otherwise, the protection for the fault on the feeder connected with PCC should be same as the protection of the other main feeders.

For the fault $F_2$, the fault on the main feeder not connected with PCC, the relays, $R_2$ and $R_3$ will trip the $CB_4$ and $CB_5$ as the binary status of $CT_4$ and $CT_5$ are '1' and since the binary status of $CT_2$, $CT_3$, $CT_6$ and $CT_7$ are all '0', the other CBs will not operate.

For the fault at the branch feeder, $F_3$, the $CB_7$ will open to isolate the fault owing to the fact that the $CT_7$'s side are marked as '1' by the relay '$R_3$' in both modes, while the other CBs in the microgrid will not be tripped as the tripping condition in Fig. 8 is not satisfied. In this protection scheme, the under-voltage protection suggested in [10] is used to provide backup in case of the failure of the transient based protection scheme. The threshold for the under-voltage element is set as 0.9 pu to ensure sensitivity to fault conditions. A time delay of 0.3 s is also implemented which provides sufficient backup protection grading margin for the transient based protection, and is acceptable for a 400 V network. The performance of the proposed strategy is validated by a benchmark microgrid presented in Section IV.

Given that many existing relays cannot handle inputs from multiple CTs, the scheme could be implemented using more than one relay with local communication capability for exchanging the values of calculated energy. In that condition, each relay calculates the energy from its own inputs and compares it to the energy results from other relays at the same busbar. In this way, the CT with maximum energy achieves the status of '1' and then, based on the coordination algorithm in Fig. 8, the fault in the network can be isolated successfully.

TABLE I
BINARY OUTPUTS FOR FAULTS $F_1$, $F_2$ AND $F_3$

| Bus/Relay Number | CTs' Number | Grid-Connected Mode | | | Islanded Mode | | |
|---|---|---|---|---|---|---|---|
| | | F1 | F2 | F3 | F1 | F2 | F3 |
| 1 | 1 | 1 | 1 | 1 | 0 | 0 | 0 |
| | 2 | 1 | 0 | 0 | 1 | 0 | 0 |
| 2 | 3 | 0 | 0 | 0 | 0 | 0 | 0 |
| | 4 | 0 | 1 | 1 | 0 | 1 | 1 |
| 3 | 5 | 1 | 1 | 0 | 1 | 1 | 0 |
| | 6 | 0 | 0 | 0 | 0 | 0 | 0 |
| | 7 | 0 | 0 | 1 | 0 | 0 | 1 |

### *B. Design of the Single-Phase Tripping Algorithm*

Single-phase-to-ground fault is the most common type of fault in the power system. Additionally, in a low-voltage microgrid, there is a large amount of the single-phase loads, therefore, tripping all phases during a single-phase-to-ground fault may not be the ideal solution [34]. As proposed in [35], in a single-phase-to-ground fault, the current in the faulted phase experiences a severe distortion compared to the healthy phases. Based on this principle, a single-phase tripping algorithm has been designed to facilitate single-phase tripping capability.

The proposed single-phase tripping algorithm has two steps, including the energy normalization and faulted phase selection. In the first step, the three-phase energy measured from the CT will be normalized by dividing the maximum phase energy of that CT as (8).

$$TWE^{p_{nor}}_{j,CT_n} = \frac{TWE^{p}_{j,CT_n}}{TWE^{p_{max}}_{j,CT_n}} \tag{8}$$

where the $TWE^{p_{nor}}_{j,CT_n}$ is the normalized phase transient wavelet energy. After normalization, in the case of a single-phase-to-ground fault, the energy of the faulted phase will equal to 1 and the energies of the other two phases range between 0 to 1. Based on the simulation, the normalized energy of the healthy phases in the worst scenarios (seen Table VI) with 40 dB noise is lower than 0.07. After considering a 50% safety margin, the phases with normalized energies less than 0.1 will be not tripped. If the above condition is not satisfied, e.g. normalized energies of 2 or more phases are above 0.1, the standard three-phase tripping will be implemented. The output of this logic can be added at the operating stage before tripping the CBs, either single-phase or three-phase.

### *C. Setting of the Thresholds, $TWE_{thr}$ and $I_{thr\_pe}$*

As discussed in [36], high frequency based protection is relatively sensitive to the noise disturbances and the wavelet transform cannot totally remove the high frequency noise. Therefore, the impact of noise on the protection performance should be considered. This has been included by introducing the threshold as shown in Fig. 7. The white noise with 40 dB signal to noise ratio (SNR), as applied in [37], was superimposed on the measured current from the CTs to represent the worst case noise pollution scenario. The $SNR_{dB}$ is defined by (9), where $P_S$ and $P_N$ are the powers of the measured signal and the injected noise respectively [38].

$$SNR_{dB} = 10log10^{\frac{P_S}{P_N}} \tag{9}$$

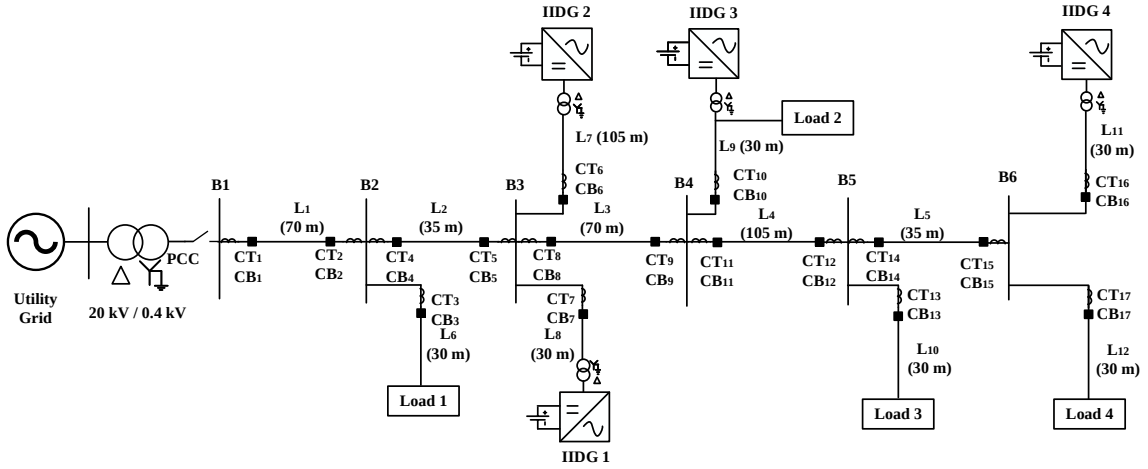


Fig. 9. The studied benchmark microgrid [39].

After injecting noise with SNR of 40 dB, the simulation revealed that the maximum energy value out of all relays in the network is around 1.3. Considering a security margin of 50%, the energy threshold is set as 2 for all relays in the network. As the energy threshold is calculated based on the maximum tolerable noise level, the proposed scheme is expected to remain stable under all noise levels with SNR values down to 40 dB. It needs to be clarified that the maximum energy related to noise depends on the real network situation, therefore, the energy threshold can be higher or lower in specific applications.

Additionally, the stability requirements under non-fault disturbances, including load switching and power variation of the generators, should be considered. The second tripping threshold, $I_{thr\_pe}$ , is introduced for the security of the branch feeder protection, to avoid false tripping caused by external disturbances. The setting of $I_{thr\_pe}$ is based on (10).

$$I_{thr\_pe} = \frac{\sqrt{2} S_{Feeder}}{\sqrt{3} V_{L\_L}} \times 1.5 \tag{10}$$

Where the $I_{thr\_pe}$ is the peak value of the setting current; $S_{Feeder}$ is the total capacity of the loads and generators connected to the local branch feeder; $V_{L-L}$ is the rated line to line voltage of the microgrid and 1.5 represents additional 50% security margin. Given that loading of any given feeder in a distribution network changes as a result of the network switching actions, e.g., one feeder switches to another feeder, during the network reconfiguration, the $S_{Feeder}$ in (10) is selected as the maximum capacity of connected loads and generators of the investigated feeder among all possible network configurations. One point which needs to be highlighted here is that the additional current threshold is only applied to the branch feeders, as shown in the algorithm flowchart in Fig. 7. This additional condition can avoid the sensitivity of the main feeder protection being compromised.

## IV. PERFORMANCE EVALUATION

### A. Benchmark Microgrid Model

For protection testing purposes, a model of a 400 V, 50 Hz, microgrid has been developed in MATLAB/SIMULINK based on the CIGRE benchmark microgrid model [39].

A single line diagram of the test network is shown in Fig. 9. The microgrid connects to a 20-kV distribution network by a step-up transformer and it can operate in both grid-connected and islanded modes by controlling the status of the breaker at PCC. The length of lines, $L_1$ to $L_{12}$, have been marked in the diagram and the detailed parameters of these feeders can be found in [39]. The CTs are installed at the ends of each feeder, therefore, the current information of all feeders, including the main feeders and the branch feeders, can be monitored. For every busbar, one relay is installed to control the operation of the CBs. As shown in Fig. 9, there are four IIDGs in the microgrid. In order to eliminate the zero-sequence current on the inverter side, the IIDG is connected to the microgrid by a star-delta connected transformer. In grid-connected mode, all IIDGs operate in active and reactive power (PQ) control mode, and only deliver the active power to the grid. When the connection with the utility grid is lost, the microgrid will be controlled based on the 'master-slave' strategy, where the control strategy of IIDG 1 will switch to voltage and frequency (VF) control mode and operate as a grid forming converter to provide the reference voltage and frequency to the islanded microgrid and the remaining three IIDGs still operate as grid following converters in the PQ mode. It should be noted that there are a number of ways to maintain stability of the microgrid energised by multiple IIDGs. For example, a droop-based control strategy can be introduced, where the frequency and voltage are regulated cooperatively by all converters in the grid [40]. However, given the proposed protection scheme relies on the fault-induced high-frequency transients rather than the properties of the generators in the network, the protection response will be largely unaffected by the way the converters regulate voltage and frequency within the islanded microgrid. Therefore, the master-slave control approach adopted in the simulation model was considered adequate for the purposes

TABLE II
PARAMETERS OF GENERATORS AND LOADS

| Equipment Type | Name | Controller Type | Rated Power (kVA) | Power Factor |
|---|---|---|---|---|
| **Generators** | IIDG 1 | PQ/VF | 20/50 | 1/slacking bus |
| | IIDG 2 | PQ | 20 | 1 |
| | IIDG 3 | PQ | 30 | 1 |
| | IIDG 4 | PQ | 40 | 1 |
| **Loads** | Load 1 | NA | 20 | 0.9 |
| | Load 2 | NA | 20 | 0.8 |
| | Load 3 | NA | 20 | 0.9 |
| | Load 4 | NA | 30 | 0.9 |

TABLE III
SCENARIOS FOR EVALUATING THE IMPACTS OF THE FAULT LOCATIONS AND TYPES

| Cases | Faulted Feeder | Fault Type | Fault Resistance | Inception Angle of Phase A | Microgrid Mode |
|---|---|---|---|---|---|
| 1 | $L_1$ | AG | 1 | 30° | Grid-Connected |
| 2 | $L_3$ | AB | 1 | 30° | Grid-Connected |
| 3 | $L_{10}$ | ABC | 1 | 30° | Grid-Connected |
| 4 | $L_1$ | AG | 1 | 30° | Islanded |
| 5 | $L_3$ | AB | 1 | 30° | Islanded |
| 6 | $L_{10}$ | ABC | 1 | 30° | Islanded |

of evaluating performance of the proposed protection scheme. The control structures of the grid-forming and grid-following converters in the microgrid are developed based on [41]. Considering the limited current generating capability of power electronic converters, the fault currents from all IIDGs have been limited to 1.2 pu as suggested in [42]. The parameters of the four IIDGs and loads are presented in TABLE II.

### *B. Impact of the Fault Location and Fault Type*

In this section, the fault scenarios in Table III are simulated to evaluate the impact of the fault position and type on the protection performance. Three types of faults, including phase A-to-ground (AG), phase A-to-B (AB) and three-phase (ABC) faults, are applied at the midpoint of the feeders $L_1$, $L_3$ and $L_{10}$, first in grid-connected, and then in the islanded mode. In this initial investigation, both fault resistance and inception angle were fixed, as indicated in the table.

As revealed by Fig. 4, after the occurrence of the fault, the value of transient wavelet energy, $TWE_j$ ,will increase to its peak value and then gradually decrease, as the averaging window moves along. The peak energy determines the maximum sensitivity of the proposed protection scheme, and therefore the peak value of the maximum phase energy, $TWE_{j,CT_n}^{P_{max}}$, is used in the sensitivity assessment, which is represented as $TWE_{CT_n}^{Peak}$. The results are displayed in Table IV and Table V. It can be seen that regardless of the type or position of the fault, the CTs closest to the fault, e.g. $CT_2$ in Cases 1 and 4, $CT_8$ and $CT_9$ in Cases 2 and 5, $CT_{13}$ in Cases 3 and 6, have the highest energy values, and the energies of the CTs at the same busbar confirm the relationship in (7).

It is worth noting that the magnitude of transient energy generated at the fault position is determined by the instantaneous value of the applied superimposed voltage and the equivalent impedance seen from the fault point. For example, in Case 2 (where the AB fault is triggered in the network), the applied voltage magnitude is equal to the system line voltage, while in Case 1 (i.e. AG fault), the applied voltage corresponds to the phase A. Additionally, the fault inception angle of line-to-line voltage $V_{AB}$ in Case 2 (i.e., 60°) is higher than the inception angle of AG fault (i.e., 30°) in Case 1. Consequently, the fault transient energy for Case 2 is expected to be higher than that observed in Case 1, which can be verified by comparing the energy of $CT_1$ and $CT_2$ in Case 1, to the energy of $CT_8$ and $CT_9$ in Case 2, as presented in Table IV and Table V. For the three-phase fault, the inception angle of phase A, phase B and phase C are 30°, −90° and 150° respectively. As explained in Section II.C, only the maximum phase energy is implemented in the developed protection algorithm, i.e., the phase B energy is the highest in Case 3. Therefore, the energy observed in Case 3 will also be greater than the energy in Case 1 owing to the impact of the increased fault inception angle, e.g., comparing the energy of $CT_1$, $CT_2$ in Case 1 (AG fault), to the energy of $CT_{13}$ in Case 3 (ABC fault). The energy generated at the fault position will propagate towards

TABLE IV
SIMULATION RESULTS OF THE FAULTS WITH DIFFERENT LOCATIONS AND TYPES (GRID-CONNECTED MODE)

| **CTs/CBs Number** | **Case1** ($L_1$) | | | **Case2** ($L_3$) | | | **Case3** ($L_{10}$) | | |
|---|---|---|---|---|---|---|---|---|---|
| | $TWE_{CT_n}^{Peak}$ | Binary Value | CB trips?/Correct? | $TWE_{CT_n}^{Peak}$ | Binary Value | CB trips?/Correct? | $TWE_{CT_n}^{Peak}$ | Binary Value | CB trips?/Correct? |
| 1 | 26.5 | 1 | Yes/Yes | 119.6 | 1 | No/Yes | 54.6 | 1 | No/Yes |
| 2 | 378.1 | 1 | Yes/Yes | 119.6 | 0 | No/Yes | 54.6 | 0 | No/Yes |
| 3 | 2.9 | 0 | No/Yes | 13.3 | 0 | No/Yes | 6.8 | 0 | No/Yes |
| 4 | 316.4 | 0 | No/Yes | 203.1 | 1 | No/Yes | 95.3 | 1 | No/Yes |
| 5 | 316.4 | 1 | No/Yes | 203.1 | 0 | No/Yes | 95.3 | 0 | No/Yes |
| 6 | 10.9 | 0 | No/Yes | 63.1 | 0 | No/Yes | 28.8 | 0 | No/Yes |
| 7 | 40.8 | 0 | No/Yes | 71.0 | 0 | No/Yes | 32.5 | 0 | No/Yes |
| 8 | 66.0 | 0 | No/Yes | 862.9 | 1 | Yes/Yes | 396.8 | 1 | No/Yes |
| 9 | 66.0 | 1 | No/Yes | 777.5 | 1 | Yes/Yes | 396.8 | 0 | No/Yes |
| 10 | 15.5 | 0 | No/Yes | 138.4 | 0 | No/Yes | 86.0 | 0 | No/Yes |
| 11 | 17.6 | 0 | No/Yes | 261.8 | 0 | No/Yes | 841.7 | 1 | No/Yes |
| 12 | 17.6 | 1 | No/Yes | 261.8 | 1 | No/Yes | 841.7 | 0 | No/Yes |
| 13 | 1.0 | 0 | No/Yes | 14.4 | 0 | No/Yes | 1831.0 | 1 | Yes/Yes |
| 14 | 10.3 | 0 | No/Yes | 154.8 | 0 | No/Yes | 196.5 | 0 | No/Yes |
| 15 | 10.3 | 1 | No/Yes | 154.8 | 1 | No/Yes | 196.5 | 1 | No/Yes |
| 16 | 3.2 | 0 | No/Yes | 49.5 | 0 | No/Yes | 73.0 | 0 | No/Yes |
| 17 | 2.1 | 0 | No/Yes | 31.4 | 0 | No/Yes | 32.2 | 0 | No/Yes |

TABLE V
SIMULATION RESULTS OF THE FAULTS WITH DIFFERENT LOCATIONS AND TYPES (ISLANDED MODE)

| CTs/CBs Number | Case4 ($L_1$) | | | Case5 ($L_3$) | | | Case6 ($L_{10}$) | | |
|---|---|---|---|---|---|---|---|---|---|
| | $TWE_{CT_n}^{Peak}$ | Binary Value | CB trips?/Correct? | $TWE_{CT_n}^{Peak}$ | Binary Value | CB trips?/Correct? | $TWE_{CT_n}^{Peak}$ | Binary Value | CB trips?/Correct? |
| 1 | 0.0 | 0 | Yes/Yes | 0.0 | 0 | No/Yes | 0.0 | 0 | No/Yes |
| 2 | 522.6 | 1 | Yes/Yes | 0.0 | 0 | No/Yes | 0.0 | 0 | No/Yes |
| 3 | 4.4 | 0 | No/Yes | 18.1 | 0 | No/Yes | 10.7 | 0 | No/Yes |
| 4 | 433.9 | 0 | No/Yes | 18.1 | 1 | No/Yes | 10.7 | 1 | No/Yes |
| 5 | 433.9 | 1 | No/Yes | 18.1 | 0 | No/Yes | 10.7 | 0 | No/Yes |
| 6 | 14.4 | 0 | No/Yes | 70.1 | 0 | No/Yes | 35.7 | 0 | No/Yes |
| 7 | 52.9 | 0 | No/Yes | 85.0 | 0 | No/Yes | 44.1 | 0 | No/Yes |
| 8 | 96.8 | 0 | No/Yes | 464.2 | 1 | Yes/Yes | 246.1 | 1 | No/Yes |
| 9 | 96.8 | 1 | No/Yes | 821.8 | 1 | Yes/Yes | 246.1 | 0 | No/Yes |
| 10 | 21.9 | 0 | No/Yes | 145.6 | 0 | No/Yes | 97.7 | 0 | No/Yes |
| 11 | 26.7 | 0 | No/Yes | 277.7 | 0 | No/Yes | 653.5 | 1 | No/Yes |
| 12 | 26.7 | 1 | No/Yes | 277.7 | 1 | No/Yes | 653.5 | 0 | No/Yes |
| 13 | 1.7 | 0 | No/Yes | 16.0 | 0 | No/Yes | 1560.0 | 1 | Yes/Yes |
| 14 | 15.1 | 0 | No/Yes | 161.8 | 0 | No/Yes | 195.8 | 0 | No/Yes |
| 15 | 15.1 | 1 | No/Yes | 161.8 | 1 | No/Yes | 195.8 | 1 | No/Yes |
| 16 | 4.3 | 0 | No/Yes | 49.6 | 0 | No/Yes | 68.2 | 0 | No/Yes |
| 17 | 3.6 | 0 | No/Yes | 34.8 | 0 | No/Yes | 34.9 | 0 | No/Yes |

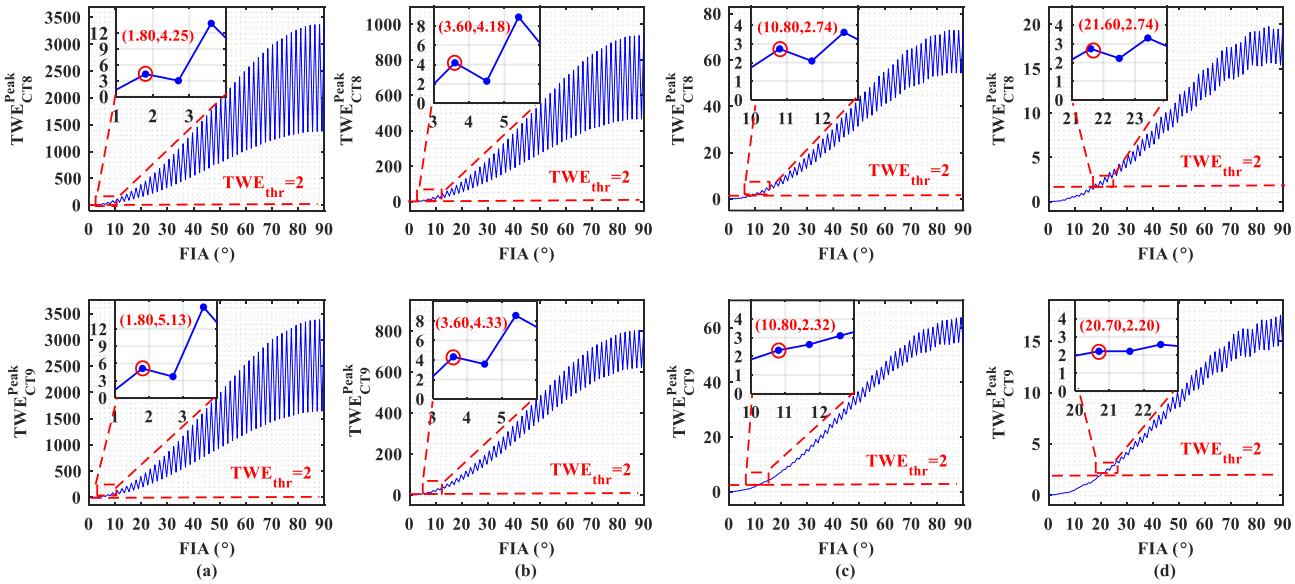


Fig. 10. The transient wavelet energies of $CT_8$ and $CT_9$ for the A-G faults in the L3 (Grid-connected microgrid), (a) 0.1 Ω, (b) 1 Ω, (c) 5 Ω, (d) 10 Ω.

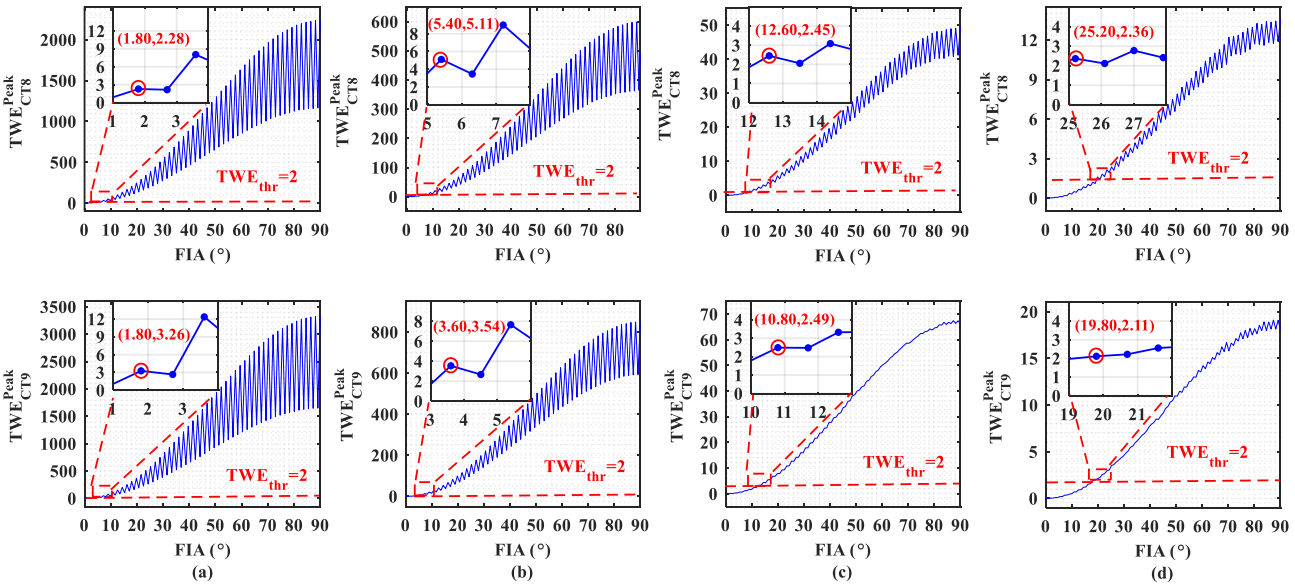


Fig. 11. The transient wavelet energies of $CT_8$ and $CT_9$ for the A-G faults in the L3 (Islanded microgrid), (a) 0.1 Ω, (b) 1 Ω, (c) 5 Ω, (d) 10 Ω.

other busbars in the network. However, the actual energy levels measured by the CTs at each busbar are subject to the attenuation introduced by the impedance of the lines, as well as of other components during the propagation process. As the proposed scheme utilizes the energy relation (7), the exact energy levels measured by the CTs are not required for correct operation of the scheme, thus the analytical energy quantification i s n ot c onducted i n t his p aper. F or t he faults at different p ositions, e .g., f eeder c onnected a t P CC (Cases 1, 4), main feeders (Cases 2, 5) and branch feeders (Cases 3, 6), the faulted feeder can be selected accurately and the CBs can operate correctly based on the strategy outlined in Fig. 8. Furthermore, in the proposed protection scheme, the tripping action of $CB_1$ is governed by the tripping signal from the relay at Bus 2, which ensures that the fault at $L_1$ in the islanded microgrid can always be isolated. The results confirm that, the proposed protection scheme operates correctly both in the grid-connected and islanded mode, and its performance is not impacted by the fault location or type. Additionally, the proposed scheme can still work if not every busbar has a relay, but there will be some loss of protection discrimination. For example, for the fault at $L_3$ in Fig. 9, if there is no relay at Bus 4, then the relay at Bus 3 and Bus 5 will operate to trip the $CB_8$ and $CB_{12}$ to isolate the fault. However, given the limited communication and computation capability of most reclosers in power system, the proposed scheme might be difficult to be implemented by reclosers.

### C. Impact of the Fault Inception Angle and Fault Resistance

As reported in [22], the energy of the fault-induced transient depends on the fault inception angle (FIA) and fault resistance. Given the single-phase-to-ground fault is most frequent, it is used in this section to evaluate the impact of fault inception angle on the transient wavelet energy. In this test, AG faults are applied at the midpoint of $L_3$. The fault inception angle ranges from 0° to 90° and the investigated fault resistances include 0.1 Ω, 1 Ω, 5 Ω and 10 Ω.

The simulation results (a total of 808 cases) are shown in Fig. 10 and Fig. 11. Theoretically, considering continuous time domain, for the faults with constant fault resistance, the energy of the fault induced transients should increase with the rise of the FIA, as indicated in [22]. However, in the designed numerical protection, where the current waveform sampling frequency is reduced to 10 kHz, the relay cannot detect all fault inception points with the same sensitivity. For the fault instances occurring between sampling points, the calculated energy is reduced due to loss of the high frequency information at such low sampling rate. To reveal the negative impact of the low sampling frequency on the measured energy, in simulation, the faults were applied with an angle increments of 0.9°, i.e. 50 $\mu s$. This means 2 points are contained between the neighbouring current samples. For these "blinded" points, the transient wavelet energy will experience a magnitude decay, which results in the periodical fluctuation o f t he transient wavelet energy as can be seen in Fig. 10 and Fig. 11. The first point with the energy higher than $TWE_{thr}$ has been highlighted in the zoomed fragment of each figure (in the top-left corner).

TABLE VI
MINIMUM DETECTABLE FIAs OF THE SCHEME

| Microgrid Mode | Fault Resistance | | | |
|---|---|---|---|---|
| | 0.1 Ω | 1 Ω | 5 Ω | 10 Ω |
| Grid-Connected | 1.8° | 3.6° | 10.8° | 21.6° |
| Islanded | 1.8° | 5.4° | 12.6° | 25.2° |

This point indicates the minimum FIAs detectable by the relay at the assumed sensitivity setting of $TWE_{thr} = 2$. For the FIAs above this point (including the points at the lower boundary), the energy is always higher than 2. Based on the coordination strategy in Fig. 8, for the fault at $L_3$, the energy values of the $CT_8$ and $CT_9$ should be both higher than $TWE_{thr}$. In this case, the protection performance under varying fault resistance is summarized as Table VI. It can be seen that for the faults with higher resistance, the protection scheme needs higher FIAs. For example, in the case of 10 Ω faults, the minimum detectable FIA is approximately 25°.

As the nominal voltage of the test system is 400 V, 10 Ω can be regarded as high fault resistance. As reported in [43], the high-frequency based scheme with minimum fault inception angle around 30° is still considered to be effective and reliable under the high-impedance fault conditions. It should be noted that the value of 10 Ω is not the maximum detectable fault resistance of the scheme. Through additional simulation studies, it was determined that with 90° fault inception angle, the scheme can detect the faults with resistances up to 27 Ω and 25 Ω in the grid-connected and islanded mode respectively. Additionally, it is clear that the values of the minimum detectable FIAs are close in both modes of operation (e.g. the angle difference in the worst-case scenario is less 3.6°), which further proves that the performance of the proposed scheme is largely unaffected by the properties of the energy sources and the operating modes of microgrid.

### D. Protection Security Under Non-Fault Disturbances

In this section, the impacts of typical non-fault transients, including load switching, motor start, and power variation of the IIDGs, are studied. The worst-case scenario in this test

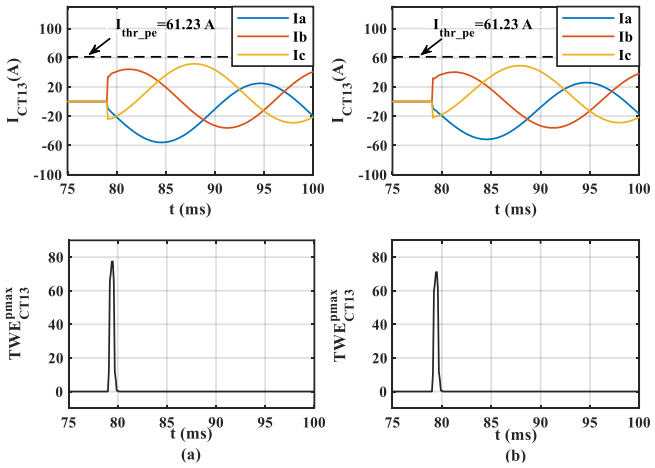


Fig. 12. The simulation results of the load 3 connection, (a) Grid-connected mode, (b) Islanded mode.

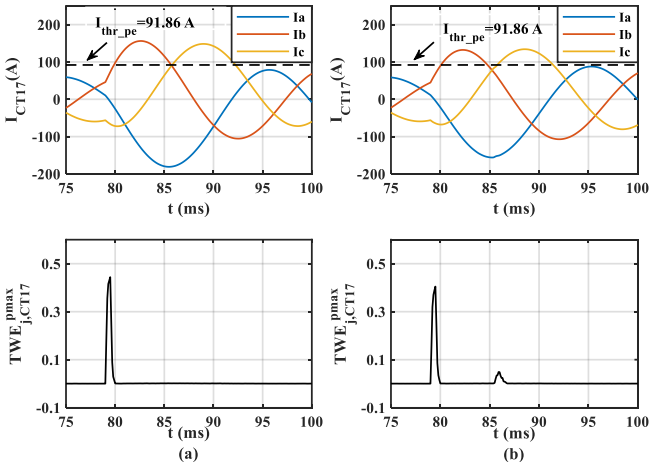


Fig. 13. The simulation results of the three-phase motor start, (a) Grid-connected mode, (b) Islanded mode.

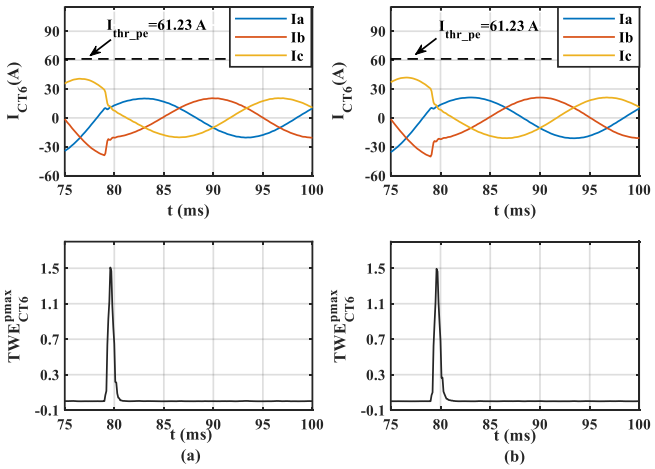


Fig. 14. The simulation results of the power variation of the IIDG 2, (a) Grid-connected mode, (b) Islanded mode.

is presented by the CT closest to the transient which has the highest energy. Therefore, the energy and current of the CT closest to the disturbance are displayed only.

The simulation results of load 3 connection in both operating modes are displayed in Fig. 12. Although the energy caused by the load connection is higher than the assumed threshold, $TWE_{thr}$, the current is lower than the defined $I_{thr\_pe}$, and therefore, the protection remains stable. To evaluate the motor start impact, a three-phase 10 kVA motor was switched on in parallel with load 4. The results are shown in Fig. 13. Large starting current is produced by the motor, which is higher than the value of $I_{thr\_pe}$, however, the unwanted tripping is avoided because the wavelet energy caused by the motor start is lower than the assumed threshold $TWE_{thr}$. Additionally, considering the uncertain nature of renewable energy based generation such as solar and wind, the power generated from the IIDG changes with the variation of the environmental condition. Therefore, the fast variation of the power generation is also considered in this test, where the generation of the IIDG 2 decreases from full loading to half loading condition in a very short period of time. The results are presented in Fig. 14. Both values of energy and current are below the corresponding thresholds, therefore, the protection scheme remains stable.

### *E. Impact of Measuring Noise*

In this section, the white noise with 40 dB SNR is superimposed on the current to evaluate the impact of the measurement noise. The energy threshold is maintained as 2, which is 1.5 times the maximum energy in the normal operating condition. The AG fault is applied in the middle of $L_3$ in both grid-connected and islanded mode of operation. From the energy diagrams in Fig. 10 and Fig. 11, with the decrease of the FIAs and the increase of fault resistance, the magnitude of the energy caused by the fault transients will be reduced. The worst-case scenarios from Table VI, where the fault resistance is 10 Ω, and the FIA equals to the minimum detectable angle, are selected for this test. The simulation results are shown in Fig. 15, where the tripping signal refers to the signal used to control the operation of the $CB_8$ and $CB_9$, which is obtained after applying the 'AND' logic to the tripping signals from relays $R_3$ and $R_4$. As can be seen in Fig.15, the energy of noise is always lower than the energy threshold in the normal state, and the proposed scheme can recognise the faulted feeder and isolate the fault correctly in both microgrid operating modes.

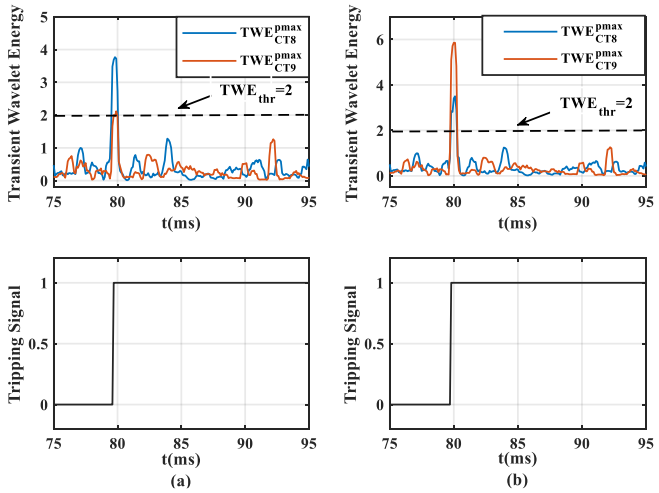


Fig. 15. The simulation results of the 40 dB noise injection, (a) Grid-connected mode, (b)Islanded mode.

### *F. Impact of IIDG Transformer Earthing Arrangement*

The simulation results presented in previous sections were obtained assuming that the IIDG interface transformer windings are star/delta connected with the transformer neutral being solidly earthed. This arrangement is often found in technical literature [11] [33] [44] and was also adopted in this paper. However, some other transformer connection practices, e.g., delta/delta connection or star/delta connection with earthing impedance, can be also used to achieve specific aims. Therefore, in this section, the impact of earthing arrangement of the IIDG transformer is investigated. The studied connections include delta/delta, and star/delta with earthing impedance (earthing resistor of 5 Ω was used in this study). The fault

TABLE VII
SIMULATION RESULTS CONSIDERING TRANSFORMERS WITH DIFFERENT EARTHING ARRANGEMENTS

| CTs/CBs Number | Grid-Connected | | | | | | Islanded | | | | | |
|---|---|---|---|---|---|---|---|---|---|---|---|---|
| | Case 1 ($L_1$) | | Case 2 ($L_3$) | | Case 3 ($L_{10}$) | | Case 4 ($L_1$) | | Case 5 ($L_3$) | | Case 6 ($L_{10}$) | |
| | $TWE^{Peak}_{CT_n}$ delta/delta star/delta (5Ω) star/delta (0Ω) | CB Trips/ Correct? | $TWE^{Peak}_{CT_n}$ delta/delta star/delta (5Ω) star/delta (0Ω) | CB Trips/ Correct? | $TWE^{Peak}_{CT_n}$ delta/delta star/delta (5Ω) star/delta (0Ω) | CB Trips/ Correct? | $TWE^{Peak}_{CT_n}$ delta/delta star/delta (5Ω) star/delta (0Ω) | CB Trips/ Correct? | $TWE^{Peak}_{CT_n}$ delta/delta star/delta (5Ω) star/delta (0Ω) | CB Trips/ Correct? | $TWE^{Peak}_{CT_n}$ delta/delta star/delta (5Ω) star/delta(0Ω) | CB Trips/ Correct? |
| | 25.9 | Yes/Yes | | | | | 0 | Yes/Yes | | | | |
| **1** | 26.5 | Yes/Yes | \ | \ | \ | \ | 0 | Yes/Yes | \ | \ | \ | \ |
| | 26.5 | Yes/Yes | | | | | 0 | Yes/Yes | | | | |
| | 195.1 | Yes/Yes | | | | | 243.4 | Yes/Yes | | | | |
| **2** | 243.9 | Yes/Yes | \ | \ | \ | \ | 299.8 | Yes/Yes | \ | \ | \ | \ |
| | 378.1 | Yes/Yes | | | | | 522.6 | Yes/Yes | | | | |
| | | | 863.1 | Yes/Yes | | | | | 455.2 | Yes/Yes | | |
| **8** | \ | \ | 862.9 | Yes/Yes | \ | \ | \ | \ | 448.9 | Yes/Yes | \ | \ |
| | | | 862.9 | Yes/Yes | | | | | 464.2 | Yes/Yes | | |
| | | | 772.4 | Yes/Yes | | | | | 803.4 | Yes/Yes | | |
| **9** | \ | \ | 777.6 | Yes/Yes | \ | \ | \ | \ | 793.9 | Yes/Yes | \ | \ |
| | | | 777.5 | Yes/Yes | | | | | 821.8 | Yes/Yes | | |
| | | | | | 1802 | Yes/Yes | | | | | 1566 | Yes/Yes |
| **13** | \ | \ | \ | \ | 1830 | Yes/Yes | \ | \ | \ | \ | 1561 | Yes/Yes |
| | | | | | 1831 | Yes/Yes | | | | | 1560 | Yes/Yes |

scenarios outlined in Table III were repeated for those two earthing arrangements to evaluate the potential impact on protection performance. The simulation results are presented in Table VII, where the energy values of CTs closest to the fault, i.e., energies of $CT_1$ and $CT_2$ in cases 1 and 4, energies of $CT_8$ and $CT_9$ in cases 2 and 5, and energies of $CT_{13}$ in cases 3 and 6, are displayed. From those results, we can see that the peak energy values under different transformer arrangements are not affected in any significant way. Only for cases 1 and 4, there is a noticeable reduction, but the absolute value is still significantly higher that the assumed threshold of 2, therefore, it can be concluded that the performance of the proposed protection scheme is largely unaffected by the transformer earthing arrangement.

## V. Conclusions

In this paper, a novel protection scheme based on the transient wavelet energy has been presented and evaluated using systematic transient simulation studies. The sensitivity of the proposed scheme is demonstrated to be largely unaffected by the fault level changes, IIDGs' control strategies, fault types and positions, operating modes of microgrid, system noise and earthing arrangement of interface transformer. Moreover, regarding protection security, it is shown that the protection remains stable under the typical non-fault disturbances. The test results also show that the proposed scheme can operate effectively against faults in both grid connected and islanded mode without adjusting any settings.

Compared to the traditional transient-based microgrid protection (e.g. travelling wave-based methods), the proposed algorithm requires much lower sampling rate (from more than 200 kHz down to around 10 kHz), while being able to maintain the sensitivity against faults within a wide range of fault inception angles. Furthermore, unlike differential protection, the proposed scheme only requires low-cost communications which is feasibly to implement in microgrids. Therefore, the proposed solution could potentially offer an effective and economic choice for microgrid protection. Potentially, it could be also used as a solution in future distribution systems with high amounts of converter-based generation, including a possibility of intentional islanding. Further research will consider wider application of the proposed scheme, such as detection of open circuit faults (a broken conductor), and a self-learning based threshold setting. Additionally, to accelerate the route to market, a real-time prototype of the high-frequency transients based relay will be developed and tested using the RTDS based Hardware-In-the-Loop platform.

## References


[1] B. Kroposki et al., "Achieving a 100% renewable grid: Operating electric power systems with extremely high levels of variable renewable energy," *IEEE Power and Energy Magazine*, vol. 15, no. 2, pp. 61–73, 2017.

[2] R. Lasseter and P. Paigi, "Microgrid: a conceptual solution," in *2004 IEEE 35th Annual Power Electronics Specialists Conference*, vol. 6, 2004, pp. 4285–4290.

[3] H. Al-Nasseri, M. Redfern, and F. Li, "A voltage based protection for micro-grids containing power electronic converters," in *2006 IEEE Power Engineering Society General Meeting*, 2006.

[4] I. Bae and J. Kim, "Reliability evaluation of customers in a microgrid," *IEEE Trans. on Power Systems*, vol. 23, no. 3, pp. 1416–1422, 2008.

[5] B. Brearley and R. Prabu, "A review on issues and approaches for microgrid protection," *Renewable and Sustainable Energy Reviews*, vol. 67, pp. 988–997, 2017.

[6] H. Laaksonen, "Protection principles for future microgrids," *IEEE Trans. on Power Electronics*, vol. 25, no. 12, pp. 2910–2918, 2010.

[7] A. Hooshyar, M. Azzouz, and E. El-Saadany, "Distance protection of lines emanating from full-scale converter-interfaced renewable energy power plants—part i: Problem statement," *IEEE Trans. on Power Delivery*, vol. 30, no. 4, pp. 1770–1780, 2015.

[8] V. Papaspiliotopoulos et al., "Hardware-in-the-loop design and optimal setting of adaptive protection schemes for distribution systems with distributed generation," *IEEE Trans. on Power Delivery*, vol. 32, no. 1, pp. 393–400, 2017.

[9] F. Coffele, C. Booth, and A. Dyśko, "An adaptive overcurrent protection scheme for distribution networks," *IEEE Transactions on Power Delivery*, vol. 30, no. 2, pp. 561–568, 2015.

[10] E. Sortomme, S. Venkata, and J. Mitra, "Microgrid protection using communication-assisted digital relays," *IEEE Trans. on Power Delivery*, vol. 25, no. 4, pp. 2789–2796, 2010.

[11] D. Mishra, S. Samantaray, and G. Joos, "A combined wavelet and data-mining based intelligent protection scheme for microgrid," *IEEE Trans. on Smart Grid*, vol. 7, no. 5, pp. 2295–2304, 2016.

[12] J. Yu et al., "Intelligent fault detection scheme for microgrids with wavelet-based deep neural networks," *IEEE Trans. on Smart Grid*, vol. 10, no. 2, pp. 1694–1703, 2019.

[13] Z. Chen, X. Pei, M. Yang, L. Peng, and P. Shi, "A novel protection scheme for inverter-interfaced microgrid operated in islanded mode," *IEEE Trans. on Power Electronics*, vol. 33, no. 9, pp. 7684–7697, 2018.

[14] A. Soleimanisardoo, H. Karegar, and H. Zeineldin, "Differential frequency protection scheme based on off-nominal frequency injections for inverter-based islanded microgrids," *IEEE Trans. on Smart Grid*, vol. 10, no. 2, pp. 2107–2114, 2019.

[15] X. Li, A. Dyśko, and G. Burt, "Traveling wave-based protection scheme for inverter-dominated microgrid using mathematical morphology," *IEEE Trans. on Smart Grid*, vol. 5, no. 5, pp. 2211–2218, 2014.

[16] X. Dong et al., "Implementation and application of practical traveling-wave-based directional protection in uhv transmission lines," *IEEE Trans. on Power Delivery*, vol. 31, no. 1, pp. 294–302, 2016.

[17] D. Percival and A. Walden, *Wavelet methods for time series analysis*. Cambridge university press, 2000, vol. 4.

[18] R. Cheney, J. Thorne, and G. Hataway, "Distribution single-phase tripping and reclosing: Overcoming obstacles with programmable recloser controls," in *2009 Power Systems Conference*, 2009, pp. 1–10.

[19] M. Vitins, "A fundamental concept for high speed relaying," *IEEE Transactions on Power Apparatus and Systems*, vol. PAS-100, no. 1, pp. 163–173, 1981.

[20] G. Benmouy and J. Roberts, "Superimposed quantities: Their true nature and application in relays, schweitzer engineering laboratories," *Inc. Pullman, WA USA, SEL USA*, vol. 199, 1999.

[21] T. Hensler, C. Pritchard, N. Fischer, and B. Kasztenny, "Testing superimposed-component and traveling-wave line protection," *Locating Faults and Protecting Lines at the Speed of Light: Time-Domain Principles Applied*, 2018.

[22] F. Costa, B. Souza, and N. Brito, "Effects of the fault inception angle in fault-induced transients," *IET generation, transmission & distribution*, vol. 6, no. 5, pp. 463–471, 2012.

[23] E. O. Schweitzer, B. Kasztenny, A. Guzmán, V. Skendzic, and M. V. Mynam, "Speed of line protection-can we break free of phasor limitations?" in *2015 68th Annual Conference for Protective Relay Engineers*. IEEE, 2015, pp. 448–461.

[24] N. Fischer, V. Skendzic, R. Moxley, and J. Needs, "Protective relay traveling wave fault location," in *11th IET International Conference on Developments in Power Systems Protection (DPSP 2012)*, 2012, pp. 1–3.

[25] C. Pang and M. Kezunovic, "Fast distance relay scheme for detecting symmetrical fault during power swing," *IEEE Trans. on Power Delivery*, vol. 25, no. 4, pp. 2205–2212, 2010.

[26] Y. Gu and M. Bollen, "Time-frequency and time-scale domain analysis of voltage disturbances," *IEEE Trans. on Power Delivery*, vol. 15, no. 4, pp. 1279–1284, 2000.

[27] R. P. Medeiros, F. Costa, and K. Silva, "Power transformer differential protection using the boundary discrete wavelet transform," *IEEE Trans. on Power Delivery*, vol. 31, no. 5, pp. 2083–2095, 2016.

[28] A. Megahed, A. Moussa, and A. Bayoumy, "Usage of wavelet transform in the protection of series-compensated transmission lines," *IEEE Trans. on Power Delivery*, vol. 21, no. 3, pp. 1213–1221, 2006.

[29] W. Gao and J. Ning, "Wavelet-based disturbance analysis for power system wide-area monitoring," *IEEE Trans. on Smart Grid*, vol. 2, no. 1, pp. 121–130, 2011.

[30] S. Song and G. Zou, "A novel busbar protection method based on polarity comparison of superimposed current," *IEEE Trans. on Power Delivery*, vol. 30, no. 4, pp. 1914–1922, 2015.

[31] "Discrete filter." [Online]. Available: https://uk.mathworks.com/help/simulink/slref/discretefirfilter.html

[32] M. Vetterli and C. Herley, "Wavelets and filter banks: theory and design," *IEEE Trans. on Signal Processing*, vol. 40, no. 9, pp. 2207–2232, 1992.

[33] J. Nsengiyaremye, B. Pal, and M. Begovic, "Microgrid protection using low-cost communication systems," *IEEE Trans. on Power Delivery*, vol. 35, no. 4, pp. 2011–2020, 2020.

[34] S. Zarei and M. Parniani, "A comprehensive digital protection scheme for low-voltage microgrids with inverter-based and conventional distributed generations," *IEEE Trans. on Power Delivery*, vol. 32, no. 1, pp. 441–452, 2017.

[35] Z. Bo et al., "A new approach to phase selection using fault generated high frequency noise and neural networks," *IEEE Trans. on Power Delivery*, vol. 12, no. 1, pp. 106–115, 1997.

[36] L. Tang, X. Dong, S. Luo, S. Shi, and B. Wang, "A new differential protection of transmission line based on equivalent travelling wave," *IEEE Trans. on Power Delivery*, vol. 32, no. 3, pp. 1359–1369, 2017.

[37] S. Azizi et al., "A traveling-wave-based methodology for wide-area fault location in multiterminal dc systems," *IEEE Trans. on Power Delivery*, vol. 29, no. 6, pp. 2552–2560, 2014.

[38] M. A. Jarrahi, H. Samet, and T. Ghanbari, "Fast current-only based fault detection method in transmission line," *IEEE Systems Journal*, vol. 13, no. 2, pp. 1725–1736, 2019.

[39] S. Papathanassiou, N. Hatziargyriou, K. Strunz *et al.*, "A benchmark low voltage microgrid network," in *Proceedings of the CIGRE symposium: power systems with dispersed generation*. CIGRE, 2005, pp. 1–8.

[40] U. B. Tayab, M. A. B. Roslan, L. J. Hwai, and M. Kashif, "A review of droop control techniques for microgrid," *Renewable and Sustainable Energy Reviews*, vol. 76, pp. 717–727, 2017.

[41] J. Rocabert, A. Luna, F. Blaabjerg, and P. Rodríguez, "Control of power converters in ac microgrids," *IEEE Trans. on Power Electronics*, vol. 27, no. 11, pp. 4734–4749, 2012.

[42] B. Kasztenny, M. V. Mynam, and N. Fischer, "Sequence component applications in protective relays–advantages, limitations, and solutions," in *2019 72nd annual conference for protective relay engineers (CPRE),(College Station, TX, USA)*, 2019, pp. 1–23.

[43] X. Dong, J. Wang, S. Shi, B. Wang, B. Dominik, and M. Redefern, "Traveling wave based single-phase-to-ground protection method for power distribution system," *CSEE Journal of Power and Energy Systems*, vol. 1, no. 2, pp. 75–82, 2015.

[44] S. F. Zarei, H. Mokhtari, and F. Blaabjerg, "Fault detection and protection strategy for islanded inverter-based microgrids," *IEEE Journal of Emerging and Selected Topics in Power Electronics*, vol. 9, no. 1, pp. 472–484, 2021.


**Di Liu** received the B.Eng. (Hons.) degree in Electronic and Electrical Engineering from the University of Strathclyde in 2018. He is currently pursuing his Ph.D. degree at the department of Electronic and Electrical Engineering, University of Strathclyde, Glasgow, U.K.

His main research interest is on converter control and protection of the future power network with high penetration of converter-interfaced resources.

**Adam Dyśko** (Member, IEEE) received the Ph.D. degree in electrical and electronic engineering from the University of Strathclyde, Glasgow, U.K., in 1998. He is currently a Senior Lecturer with the Department of Electronic and Electrical Engineering, University of Strathclyde. He teaches a variety of electrical engineering subjects and has been leading several research projects with both academic and industrial partners. His research interests include power systems protection, control, and stability, and power quality.

**Qiteng Hong** (Senior Member, IEEE) is currently a Senior Lecturer (Associate Professor) at the University of Strathclyde, Glasgow, U.K. His main research interest is on power system protection and control in future networks with high penetration of renewable generation. He received his B.Eng. (Hons) and Ph.D. degree in Electronic and Electrical Engineering in 2011 and 2015 respectively, both from the University of Strathclyde. Dr Hong is a member of IEEE Working Group P2004 and IEEE Task force on Cloud-Based Control and Co-Simulation of Multi-Party Resources in Energy Internet, and he also was a Regular Member of the completed CIGRE WG B5.50.

**Dimitrios Tzelepis** (Member, IEEE) received the BEng degree (Hons.) in electrical engineering from the Technological Education Institution of Athens, Athens, Greece, in 2013, and the MSc degree in wind energy systems and the PhD degree from the University of Strathclyde, Glasgow, U.K., in 2014 and 2017, respectively. He is currently a Research Fellow with the Department of Electronic and Electrical Engineering, University of Strathclyde. His research interests include power system protection, automation and control of future electricity grids, incorporating increased penetration of renewable energy sources, and high voltage direct current interconnections. His main research methods include implementation of intelligent algorithms for protection, fault location and control applications, including the utilisation of machine learning methods and advanced and intelligent signal processing techniques. He is also interested in the application, control and protection of hybrid AC/DC grids including super-conducting feeders, non-homogeneous transmission lines, and advanced sensing technologies. Additionally, he is investigating potential solutions towards the optimised performance of active distribution networks both in off-grid and on-grid modes, to facilitate a wide suite of grid services and control capabilities.

**Campbell D. Booth** received the B.Eng. and Ph.D. degrees in electrical and electronic engineering from the University of Strathclyde, Glasgow, U.K., in 1991 and 1996, respectively. He is currently a Professor and the Head of the Department for Electronic and Electrical Engineering, University of Strathclyde. His research interests include power system protection; plant condition monitoring and intelligent asset management; applications of intelligent system techniques to power system monitoring, protection, and control; knowledge management; and decision support systems.